This paper appears in IEEE Transactions on Microwave Theory and Techniques
Vo. 72, no. 11, 2024
https://doi.org/10.1109/TMTT.2024.3403772

A Simplified Formulation of the Reflection Coefficient of an Open-Ended Coaxial Probe in Multilayered Media

Hossein Asilian Bidgoli[1], Nicola Schieda[2], and Carlos Rossa[1]

***Abstract*—Permittivity spectroscopy can discern a material's composition based on its response to electromagnetic field. The predominant method employed for permittivity spectroscopy relies on measuring the reflection coefficient of an open-ended coaxial probe immersed in the material under test. While several physics-based models exist to describe the observed reflection coefficient as a function of the material properties, they assume a single, homogeneous layer. However, most applications, particularly in biomedical engineering, often involve heterogeneous media composed of layers of different permittivities.**

This paper addresses a gap in the literature and introduces a new model designed for accurately estimating the reflection coefficient of two-layer media using open-ended coaxial probe. Adapting a full-wave model initially developed for determining the reflection coefficient of homogeneous media, the proposed model incorporates the influence of second layer by expanding the spherical waves generated by the probe into planar waves using Bessel-based formulation. The proposed method is validated experimentally in different scenarios within a frequency range of 1 GHz to 5 GHz. The experimental results indicate that the proposed model can predict the reflection coefficient of the media with an error no higher than 5%, while the average error in the extracted permittivity from the inverse problem is 1.08%.

***Index Terms*—Permittivity spectroscopy, open-ended coaxial probe, modelling, reflection coefficient, multilayer medium.**

I. INTRODUCTION

PERMITTIVITY spectroscopy can characterize a medium's composition from its polarisability when subjected to an alternating electromagnetic field (EMF) of varying frequency. Permittivity spectroscopy has applications across a wide spectrum of fields, especially in biomedical engineering, where the ability to distinguish between cancerous and healthy tissues using permittivity measurements has gained a lot of attention recently [1]–[4].

The most commonly employed method for permittivity spectroscopy involves transmission of a transverse electromagnetic (TEM) wave into the medium through an open-ended coaxial probe. Upon the wave's arrival at the aperture, a portion of it is immediately reflected back toward the source at the end of the probe due to the impedance mismatch between the transmission line and the medium. The remaining portion of the wave propagates through the medium.

In addition to the TEM mode, coaxial lines can support higher-order modes, such as transverse electric (TE) and transverse magnetic (TM) modes. These modes have more complex field distributions propagating in the radial and axial directions within the coaxial structure. When the primary mode is incident upon the probe's aperture, these higher-order modes are also excited. However, these modes are evanescent, meaning they do not extend to the distal end of the coaxial probe and cannot be experimentally measured.

The ratio of the amplitude of the reflected wave to the transmitted wave is the so-called reflection coefficient of the medium, which increases with the ratio of the impedance mismatch. By analyzing the observed reflection coefficient, the permittivity of the medium can be inferred. The measured reflection coefficient represents the reflection of the primary mode. However, to extract the permittivity with sufficient accuracy, the model must account for the reflection coefficients of all modes when striving for better measurement accuracy [5]–[9].

Various approaches have been proposed to link the reflection coefficient, measured with a vector network analyser (VNA), to the material's permittivity. One common method is Lumped equivalent circuit [10]–[13]. The lumped circuit represents the impedance terminating the coaxial line, which depends on the permittivity of the material. The circuit commonly includes a capacitance and a conductance to represent the fringing field and the radiation into the material, respectively [14]. While straightforward, this method offers limited accuracy. As mentioned, the aperture fields can be represented as the summation of the TEM mode and a series of TM modes. In this technique, only TEM mode is modelled by the circuit elements [15]. Consequently, it is only applicable to low value of frequency and permittivity ranges.

Various admittance models have also been proposed. The models formulations is derived by equating the magnetic fields inside and outside of the coaxial probe at the aperture [16]. These models cover a wider range of frequency and permittivity as are developed by the analytical solution of the coaxial probe [17]. However, as they only treated the TEM modes and not higher order ones, their accuracy might still be limited to materials having a high permittivity value or when using probes with small diameters. By employing a quasi-static approximation of these admittance models, some authors proposed a closed form solution [18]–[20]. While closed form

---

[1] H. Asilian and C. Rossa are with the Department of Systems and Computer Engineering, Carleton University, Ottawa, ON, Canada

[2] N. Schieda is with the Department of Radiology, Radiation Oncology and Medical Physics, University of Ottawa, Ottawa, ON, Canada

This research is supported by the Cancer Research Society and the Canadian Institutes of Health Research (grant #944486).

Cette recherche est appuyée par la Société de recherche sur le cancer et les Instituts de recherche en santé du Canada (subvention no 944486).

solutions have a lower accuracy than integral form admittance models, their computational complexity is much lower.

In contrast, full-wave methods consider both the TEM as well as higher order TM modes by equating more than one magnetic modes at the aperture through a system of equations [21]. While they deliver significantly better accuracy compared to equivalent circuit methods and encompass a wider range of frequencies and permittivity values, they hinge on the fundamental assumption that the probe interfaces with a single-layered, homogeneous medium.

Modelling the reflection coefficient of an open-ended transmission line in a heterogeneous medium has received limited attention and still presents a particular challenge. In fact, many applications of permittivity spectroscopy deal with multilayered media (e.g., biomedical tissue). Still, most studies neglect the impact of additional layers or a thin layer in between the probe's tip and the target material [5], [22]. For example, several studies have investigated the minimum thickness of a material layer required to maintain model accuracy. This is determined by placing the probe's aperture in the first layer of a 2-layer medium and monitoring the changes in the extracted permittivity as the thickness of the first layer is changed. The consensus of these studies is that the minimum thickness of the first layer must be at least the same as the probe's diameter. This way, the second layer has a negligible influence in the observed reflection coefficient. However, if this ideal experimental condition cannot be maintained, the model loses its accuracy and validity. Only a limited number of studies have tackled the issue of multilayered media analytically [23]–[27]. Specifically, [23] takes into account the excitation of different wave modes, i.e., surface, radiative, and radial guided waves, in the layered media to accurately determine the electromagnetic properties of the material over a wide frequency band. However, as it focuses on measuring both the permittivity and permeability of a material, it requires two sets of measurements. In [24] an impedance model of the coaxial line inside a two-layer material is proposed but it ignores the effect of higher order modes. [25] presents a technique to model the reflection coefficient of thin materials by considering only the fundamental coaxial mode, however the experimental measurements also indicate that this technique cannot accurately determine the loss factors of low-loss dielectric materials and, at relatively high frequencies, a full-wave model is needed for high-permittivity measurements. Furthermore, it is only applicable when the material is backed by a short-circuit termination.

Another approach involves expanding on the boundary condition equation at the aperture of the probe by leveraging the orthogonality property of the Bessel function [27]. The result of this manipulation is a system of equations that is used to solve for the reflection coefficients of N modes. However, this method requires the calculation of $N(N+1)$ infinite integrals for each measurement point, making it time-consuming. Given the demand for accurate and real-time measurements in certain applications, a faster model would be more suitable but handling layered media remains an area that requires further research.

This paper introduces a simplified mathematical model to determine the reflection coefficient of two-layer media using an open-ended coaxial probe. The proposed model is based on a full wave method originally developed for single-layer media with adjustments made to deal with multi-layer media. This involves accounting for the reflection of the radiated waves back into the probe from the second layer. The waves radiated from the probe are spherical waves, making the calculation of the reflection from the interface complicated. To address this, we employ a Bessel-based formulation to transform the radial waves into planar waves. This facilitates analysis of wave interference with the second layer and the wave reflection happening between the probe and the interface. Since the full wave method includes all the existing modes within the coaxial probe, the point matching method is then used to solve a system of equations from which the reflection coefficient is calculated. Unlike previous methods, the use of point matching method is new for multi-layer media and results in a system of equations that requires N fewer infinite integrals compared to [27]. The model is validated in two different experimental scenarios in a frequency range of 1 GHz to 5 GHz. The results show that the model can predict the reflection coefficient of 2-layer media with an error that does not exceed 5%. In a second set of experiments, it is shown that the model can also accurately determine the distance between the probe's aperture and the interface between the tissue layer with an average error of 4%. The measured reflection coefficient has also been utilized in an inverse problem to extract the permittivity of the first layer using the proposed two-layer model. This yields results with an average error of less than 1.08% across frequency spectrum. Comparing these results with the results of single layer model, which demonstrates errors of 32.6% or higher at the same distances highlights the significant improvement in accuracy.

The paper is structured as follows: Section II offers a comprehensive overview of the single-layer model. Section III outlines the contribution made to the single-layer model and how it is adapted to multi-layered media. Section IV presents the point-matching approach. Section V conducts experimental validation of the model, comprising two scenarios totaling 1608 measurement points, divided into two subsections. The first subsection compares model results with the measured reflection coefficient, while the second subsection applies measured results in two inverse problems: distance extraction and permittivity extraction. Conclusions and recommendations for potential applications of the proposed model follow in the subsequent section.

II. Reflection Coefficient Model of Coaxial Probe in a Single-layer Medium

Fig. 1(a) illustrates a coaxial probe having an aperture in contact with a material of permittivity ϵ_{m1}. Adjacent to the first material, at a distance of ℓ_1 from the probe, is a second material, which has permittivity ϵ_{m2} and extends infinitely along the z-axis. Extensive research has addressed the forward problem, that is, to calculate the reflection coefficient of the probe in the absence of the second layer while considering that the first layer extends indefinitely along the z-axis [21], [28],

[29]. However, in order to determine the reflection coefficient of the coaxial probe in a multilayered medium, as in Fig. 1(a), it is essential to revisit and expand upon the single-layer problem.

The configuration shown in Fig. 1(a) in the absence of the second layer can be divided into two regions: the left side of the xy-plane (negative z-axis), where the coaxial probe is located, and the right side of the xy-plane, where the material under test (MUT) is positioned. The wave propagation inside and outside the coaxial probe is best explained using cylindrical coordinates, as illustrated in Fig. 1(b). The coordinate system's origin is located at the center of the coaxial aperture, and the radial distance and azimuth angle are denoted by ρ and ϕ, respectively.

Consider that the coaxial probe is excited with a transverse electromagnetic (TEM) wave. The propagation of this wave along the $+z$ direction is given by $e^{-\gamma_0 z}$, where γ_0 is the propagation factor. The relative intensity of the wave at any point in the transverse plane can be represented by the radial function $f_0(\rho)$; the intensity is independent of ϕ since the TEM is symmetric about z. When the wave reaches the probe's aperture at $z = 0$, a portion of it is reflected back from the probe/material interface at a rate that depends on the reflection coefficient, denoted by $R_0 \in \mathbb{C}$.

Additionally, besides the primary TEM mode, higher-order modes are created and reflected back at the aperture. These higher-order modes are exclusively transverse magnetic (TM) modes, due to rotational symmetry [28]. The propagation factor and radial function of these higher-order modes are denoted by γ_n and $f_n(\rho)$, respectively. The reflection coefficient of a mode of order n, denoted $R_n \in \mathbb{C}$, represents the ratio of the amplitude of the reflected transverse electric field of mode n to the incident electric field.

Apart from the reflected wave, the aperture radiates the remaining portion of the TEM further into the medium. In this context, our focus is to determine the reflection coefficient R_0 associated with the non-evanescent dominant mode, which is the sole mode that can be measured experimentally. Consequently, R_0 is determined by satisfying the boundary condition at $z = 0$, where the transverse electromagnetic field inside the probe equates to the radiated magnetic field outside of the probe. The equations for these fields within and outside of the probe will be derived in the next subsections.

A. Transverse Electric and Magnetic Fields inside the Probe

The total incident and reflected transverse electric fields $E_\rho(\rho, z)$ inside the coaxial cable can be expressed as:

$$E_\rho(\rho, z) = A_0 \left[f_0(\rho) \mathrm{e}^{-\gamma_0 z} + \sum_{n=0}^{\infty} R_n f_n(\rho) \mathrm{e}^{\gamma_n z} \right], \quad (1)$$

where the subscript ρ denotes radial direction of the transverse electric field, and A_0 is the amplitude of the primary mode of the electric field. For simplicity, the temporal dependence is dropped. In (1), and in the following equation, the first term represents the incident wave, while the summation represents the total reflected wave.

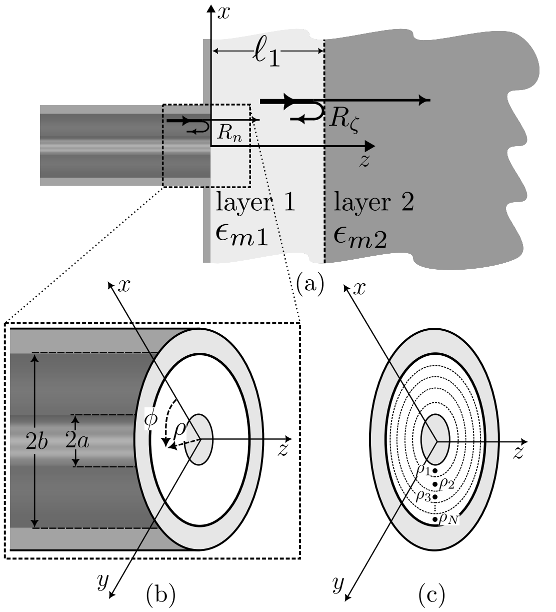

Fig. 1. (a) Open-ended coaxial probe in contact with layer 1 having permittivity ϵ_{m1} and at a distance ℓ_1 from layer 2 having permittivity ϵ_{m2}. The probe's reflection coefficients are denoted by R_n, and the differential reflection coefficient from the interface between layers 1 and 2 is R_ζ. (b) Perspective view of the coaxial probe aperture in cylindrical coordinates ρ, ϕ, and z direction with origin at the centre of the aperture. a and b are the inner and outer radii of the probe. (c) The probe aperture is divided into N discrete sections, with the middle of each section denoted as ρ_n.

The total magnetic field $H_\phi(\rho, z)$ inside the probe is:

$$H_\phi(\rho, z) = j\omega\epsilon_0\epsilon_c A_0 \left[\frac{f_0(\rho)}{\gamma_0} \mathrm{e}^{-\gamma_0 z} - \sum_{n=0}^{\infty} R_n \frac{f_n(\rho)}{\gamma_n} \mathrm{e}^{\gamma_n z} \right] \quad (2)$$

where the subscript ϕ denotes the magnetic field in the azimuthal direction, ω is the radial frequency, ϵ_c is the relative permittivity of the dielectric inside the probe, and ϵ_0 is the vacuum permittivity.

For the primary mode, the radial function is defined as

$$f_0(\rho) = \frac{N_0}{\rho}, \quad (3)$$

where the normalization factor N_0 is

$$N_0 = 1/\sqrt{\ln(b/a)} \quad (4)$$

In the above, a and b are the inner and outer radii of the probe, respectively, as shown in Fig. 1(b). The propagation factor of the primary mode is:

$$\gamma_0 = j\sqrt{\epsilon_c}(\omega/c_0) \quad (5)$$

For higher order modes, $f_n(\rho)$ can be calculated as

$$f_n(\rho) = N_n \left[J_1(p_n\rho) Y_0(p_n a) - Y_1(p_n\rho) J_0(p_n a) \right], \quad (6)$$

where J_m and Y_m denote the Bessel functions of the first and second kind, respectively, with an order of m. The eigenvalues, represented as p_n, are the roots of

$$Y_0(p_n a) J_0(p_n b) = J_0(p_n a) Y_0(p_n b) \quad n > 0. \quad (7)$$

In (6), the normalization factor N_n of higher order modes is

$$N_n = \frac{\pi p_n}{\sqrt{2}} \left[\frac{J_0^2\left(p_n a\right)}{J_0^2\left(p_n b\right)} - 1 \right]^{1/2} \qquad n > 0 \tag{8}$$

Now, the propagation factor γ_n in (1) and (2) can be defined as:

$$\gamma_n = \sqrt{p_n^2 - \epsilon_c(\omega/c_0)^2} \quad n > 0 \tag{9}$$

This equation above reveals that higher-order modes in (2) are evanescent inside the probe ($z < 0$), as their propagation factors γ_n are real positive values assuming a lossless coaxial line. In other words, none of the reflected waves with orders higher than $n = 0$ reaches the other side of the probe. Only the dominant mode ($n = 0$) propagates along the z-axis, as its propagation factor in (5) is purely imaginary. Therefore, the primary mode is the only measurable reflected wave.

Now that the equations for the fields inside the coaxial cable are defined, the subsequent subsection will present the equations for the radiated fields outside of the probe.

B. Radiated Magnetic Field Outside of the Probe

The open-ended coaxial probe can be regarded as an aperture radiating into a medium on the positive side of the z-axis, as in Fig. 1(a) and (b). The radiated magnetic can be related to the tangential electric field $E_\rho(\rho', \phi')$ at $z = 0$ at the aperture. Hereafter, prime denotes the coordinates of the source point. Since there is no geometry variation in the ϕ' direction, it follows that $E_\rho(\rho', \phi') = E_\rho(\rho')$.

The total magnetic field is the integral of all transverse magnetic fields over the aperture, that is, from $\rho = a$ to $\rho = b$ and $\phi = 0$ to $\phi = 2\pi$. The detailed analysis of the radiated magnetic field resulting from the aperture fields is extensively discussed in [28] and given as:

$$H_\phi(\rho, z) = \frac{jk_1^2}{2\pi\omega\mu_0} \int_a^b E_\rho\left(\rho'\right) \rho' \mathrm{d}\rho' \int_0^{2\pi} \frac{e^{-jkr}}{r} \cos\psi \mathrm{d}\psi \tag{10}$$

where $k_1 = \sqrt{\epsilon_{m1}(\omega/c_0)}$ is the wavenumber of the material, $\psi = \phi - \phi'$ and $r = \sqrt{\rho^2 - \rho^2 - 2\rho\rho\prime \cos\psi + z^2}$.

As mentioned earlier, this paper expands upon the method presented in [21] to accommodate layered materials, which requires calculating the reflection of the electric and magnetic fields radiated from other layers. However, determining the reflection from a flat interface using the formulation posed in (10) is not straightforward. This is due to the integration over magnetic fields propagating along the radius of a sphere, with the source points (ρ', ϕ') as their centres. This introduces complications when the incident wave reaches the flat surface of the second material obliquely.

Instead of computing the magnetic field $H_\phi(\rho, z)$ by integrating of fields radiating in r direction, as in (10), we propose to use the Sommerfeld identity [28]. This formulation allows the magnetic field to be expressed as an integration of Bessel functions propagating along the z-axis rather than along the r direction. This modified approach enables the model to consider the reflection from a flat interface with normal incidence. Further discussion on this topic will be provided later.

Consequently, with the proposed new formulation the resulting radiated magnetic field from the aperture, using the Sommerfeld identity in (10), can be expressed as:

$$\begin{aligned} H_\phi(\rho, z) = j\omega\epsilon_0\epsilon_{m1} \int_a^b E_\rho\left(\rho'\right) \rho' \mathrm{d}\rho' \\ \int_0^\infty \frac{\left(e^{-|z|\sqrt{\zeta^2 - k_1^2}}\right) J_1(\zeta\rho) J_1\left(\zeta\rho'\right) \zeta}{\left(\zeta^2 - k_1^2\right)^{1/2}} \mathrm{d}\zeta \end{aligned} \tag{11}$$

where ζ is the continuous eigenvalue. In this equation, the integration of ρ' is performed from a to b, while the integration of ζ is performed from 0 to ∞. It should be noted that, at this point, (11) applies only when there is one material present along the positive z-axis.

The boundary condition at $z = 0$ imposes that the tangential magnetic fields are continuous at the aperture, thus:

$$H_\phi(\rho, z = 0^-) = H_\phi(\rho, z = 0^+). \tag{12}$$

As such, one can replace the electric field at the aperture $E_\rho(\rho')$ in (11) with the one given by (1), and set $z = 0$ in the resulting equation, which yields:

$$\begin{aligned} H_\phi(\rho, z = 0^+) = j\omega\epsilon_0\epsilon_{m1} \int_a^b A_0 \left[f_0(\rho') + \sum_{n=0}^{\infty} R_n f_n(\rho') \right] \rho' \mathrm{d}\rho' \\ \cdot \int_0^\infty \frac{J_1(\zeta\rho) J_1\left(\zeta\rho'\right) \zeta \mathrm{d}\zeta}{(\zeta^2 - k^2)^{1/2}} \end{aligned} \tag{13}$$

Equating (2) and (13) and simplifying the resulting equation gives:

$$\begin{aligned} \epsilon_{m1} \int_a^b \left[f_0(\rho') + \sum_{n=0}^{\infty} R_n f_n(\rho') \right] \rho' \mathrm{d}\rho' \int_0^\infty \frac{J_1(\zeta\rho) J_1\left(\zeta\rho'\right) \zeta \mathrm{d}\zeta}{(\zeta^2 - k^2)^{1/2}} \\ = \epsilon_c \left[\frac{f_0(\rho)}{\gamma_0} - \sum_{n=0}^{\infty} R_n \frac{f_n(\rho)}{\gamma_n} \right]. \end{aligned} \tag{14}$$

After rearranging the terms related to the incident wave on the right side and the terms related to the reflected waves on the left side, we obtain the following equation:

$$\begin{aligned} \sum_{n=0}^{\infty} R_n \left[\frac{f_n(\rho)}{\gamma_n} + \frac{\epsilon_{m1}}{\epsilon_c} \int_a^b f_n(\rho') \rho' \mathrm{d}\rho' \int_0^\infty \frac{J_1(\zeta\rho) J_1\left(\zeta\rho'\right) \zeta \mathrm{d}\zeta}{(\zeta^2 - k^2)^{1/2}} \right] \\ = \frac{f_0(\rho)}{\gamma_0} - \frac{\epsilon_{m1}}{\epsilon_c} \int_a^b f_0(\rho') \rho' \mathrm{d}\rho' \int_0^\infty \frac{J_1(\zeta\rho) J_1\left(\zeta\rho'\right) \zeta \mathrm{d}\zeta}{(\zeta^2 - k^2)^{1/2}} \end{aligned} \tag{15}$$

Dividing both sides of this equation by the right-hand side yields:

$$\sum_{n=0}^{\infty} R_n W_n = 1 \tag{16}$$

In which W_n is equal to:

$$W_n = \frac{f_n(\rho)/\gamma_n + \left(\epsilon_m/\epsilon_c\right) I_n}{f_0(\rho)/\gamma_0 - \left(\epsilon_m/\epsilon_c\right) I_0} \tag{17}$$

And I_n is:

$$I_n = \int_0^\infty \frac{J_1(\zeta\rho)\zeta}{\sqrt{\zeta^2 - k_1^2}} \cdot \int_a^b f_n\left(\rho'\right) J_1(\zeta\rho')\rho' d\rho' d\zeta\,. \tag{18}$$

This equation deviates from past literature. In previous studies, the integration was performed over both (ρ',ϕ'), representing the coordinates of the source points within the aperture [21]. However, in the proposed approach the last integral is expressed in terms of Bessel functions over a continuous eigenvalue ζ. This implies that instead of integrating over spherical waves, the integration is carried out over plane waves with different propagation factors. As we will observe later, this formulation simplifies the analysis for measuring two-layer materials significantly, while maintaining modeling accuracy.

Equation (16) provides the normalized weight coefficients W_n corresponding to the reflection coefficients (R_n) at a given ρ on the aperture. The derived equations in this section need to be revised to incorporate the effect of the second layer. This will be addressed in the following section, which begins with the calculation of the reflection coefficient of the Layer1/Layer2 interface. Subsequently, we will update the Layer1 magnetic equation $H_\phi(\rho, z = 0^+)$ while considering the reflections that exist between the aperture and the interface.

III. Reflection Coefficient Model of Coaxial Probe in Two-Layered Media

The method discussed in the previous section is only valid when the same material extends infinitely along the z-axis at the aperture of the probe. If the material in contact with the probe has a finite length in the z direction and shares a boundary with a second material at $z = \ell_1$, as illustrated in Fig. 1, the electromagnetic wave the probe emits is reflected at this interface. Depending on the values of ℓ_1, ϵ_{m1}, and ϵ_{m2}, this reflection can significantly impact the measurement of R_0 [30]. It is, therefore, necessary to consider this interface when calculating R_0 in multilayer media. Previous work derive the reflection coefficient of the interface between the layers by simultaneously solving the boundary conditions of the electric and magnetic fields at the aperture [23], [27]. In contrast, in this paper, successive reflections of the magnetic field between the layer's interface and the probe are added to determine the total magnetic field, from which the interface's reflection coefficient is determined. This approach provides a better insight into how the second layer affects the radiated magnetic field.

A. Reflection Coefficient of Layer1/Layer2 Interface

The motivation behind the newly proposed formulation using the Sommerfeld identity in (11) is to aid in determining the effect of the interface reflection coefficient at the aperture. In the literature, in the case of a magnetic field in the form of (10), the radiation occurs in the direction of r for every source point (ρ', ϕ'). This wave changes direction with every oblique incident and continues to reflect back and forth as will be discussed in subsequent sections [31]. Incorporating these waves into the calculation of the reflection coefficient introduces additional complexity.

The incident wave at the interface of the two material layers is a radiated TM wave originating from the aperture. Taking the derivative of the magnetic field in (11) with respect to the continuous eigenvalue ζ yields a differential wave characterized by a wave number of $\gamma_\zeta = (\zeta^2 - k^2)^{1/2}$. This differential wave travels along the z-axis, representing a normal incident of a traveling wave toward the material interface. For each specific wave number, the complex part of the interface reflection coefficient will be different. Hence, it is important to consider the variation in the reflection coefficient based on the specific wave number. By integrating the updated differential magnetic field over ζ while taking into account the aperture and interface reflection, the magnetic field can be accurately calculated.

The differential incident magnetic field, obtained by taking the derivative of (11) with respect to ζ is expressed as:

$$\partial H_{\phi i}(\rho, z) = H_\zeta(\rho) e^{-j\gamma_{\zeta 1} z} \tag{19}$$

where $H_\zeta(\rho)$ represents the magnetic radial function for every ζ, and $\gamma_{\zeta 1}$ is the propagation factor related to every ζ in the first layer. Given the following relationships between the electric and magnetic fields in the two tissue layers:

$$\begin{aligned} j\omega\epsilon_0\epsilon_{m1} E_{\rho i}(\rho, z) &= -\frac{\partial}{\partial z} H_{\phi i}(\rho, z), \quad 0 < z < \ell_1 \\ j\omega\epsilon_0\epsilon_{m2} E_{\rho i}(\rho, z) &= -\frac{\partial}{\partial z} H_{\phi i}(\rho, z), \quad \ell_1 < z, \end{aligned} \tag{20}$$

the differential electric field can also be written as:

$$\partial E_{\phi i}(\rho, z) = -j\frac{\gamma_{\zeta 1}}{\omega\epsilon_0\epsilon_{m1}} H_\zeta(\rho) e^{-j\gamma_{\zeta 1} z}. \tag{21}$$

These incident waves are partly reflected back by the interface with a reflection coefficient of R_ζ. The differential electric and magnetic component of this reflected wave in the first layer, ∂E_{pr} and $\partial H_{\phi r}$, respectively, can be written as:

$$\begin{aligned} \partial E_{\rho r}(\rho, z) &= -j\frac{\gamma_{\zeta 1}}{\omega\epsilon_0\epsilon_{m1}} R_\zeta H_\zeta(\rho) e^{j\gamma_{\zeta 1} z} \\ \partial H_{\phi r}(\rho, z) &= -R_\zeta H_\zeta(\rho) e^{j\gamma_{\zeta 1} z} \end{aligned} \tag{22}$$

These waves are also partly transmitted to the second layer. The amplitude of the transmitted waves in relation to the incident waves can be represented by a transmission coefficient denoted as T_ζ. Therefore, the transverse components of the transmitted waves in the second region are as follows:

$$\begin{aligned} \partial E_{\rho t}(\rho, z) &= -j\frac{\gamma_{\zeta 2}}{\omega\epsilon_0\epsilon_{m2}} T_\zeta H_\zeta(\rho) e^{-j\gamma_{\zeta 2} z} \\ \partial H_{\phi t}(\rho, z) &= T_\zeta H_\zeta(\rho) e^{-j\gamma_{\zeta 2} z} \end{aligned} \tag{23}$$

where $\gamma_{\zeta 2}$ is the propagation factor in the second layer. A longitudinal electric field also exists in these two layers. However, only the transverse component is needed in order to calculate the reflection coefficient. The components of the wave are tangential to the boundary of the two layers and need to be continuous across it, which means:

$$\begin{aligned} \partial E_{\rho i}(\rho, z = \ell_1) + \partial E_{\rho r}(\rho, z = \ell_1) &= \partial E_{\rho t}(\rho, z = \ell_1) \\ \partial H_{\phi i}(\rho, z = \ell_1) + \partial H_{\rho r}(\rho, z = \ell_1) &= \partial H_{\phi t}(\rho, z = \ell_1) \end{aligned} \tag{24}$$

Replacing (19), (22) and (23) in (24), and simplifying the resulting equation leads to:

$$\begin{aligned} \frac{\gamma_{\zeta 1}}{j\omega\epsilon_0\epsilon_{m1}}(1 + R_\zeta) &= \frac{\gamma_{\zeta 2}}{j\omega\epsilon_0\epsilon_{m2}} T_\zeta \\ 1 - R_\zeta &= T_\zeta \end{aligned} \tag{25}$$

Solving for the reflection coefficient using the above two equations results in:

$$R_\zeta = \frac{\gamma_{\zeta 2}/\gamma_{\zeta 1} - \epsilon_{m2}/\epsilon_{m1}}{\gamma_{\zeta 2}/\gamma_{\zeta 1} + \epsilon_{m2}/\epsilon_{m1}} \tag{26}$$

This equation provides the reflection coefficient of the differential incident wave from the layer1/layer2 interface. In order to account for the influence of the second layer on the coaxial probe measurement, it is necessary to update the magnetic wave at the aperture using (26). Subsequently, the model will be redefined, as explained in the following section.

B. Aggregated Reflection Coefficient of Probe/Layer 1/Layer 2

To determine the aggregated reflection coefficient from all interfaces seen at the probe's aperture, the total accumulated differential magnetic wave at that point, which includes multiple waves reflected from all interfaces, needs to be calculated.

Referring now to Fig. 2, as the radiated wave $\partial H_{\phi i}$ exits the probe, it propagates toward the interface between layers 1 and 2, and its magnitude at any point along z between the probe and the layer's interface is given by (19). Once the wave reaches the layer's interface, part of the wave is reflected back toward the probe. If the magnetic reflection coefficient at that point is $-R_\zeta$, the magnitude of the reflected magnetic wave as it returns to the aperture becomes $-R_\zeta H_\zeta(\rho) e^{\gamma_{\zeta 1}(z-2\ell_1)}$. Notice that z changes sign since the wave travels back, and a spatial offset of $-2\ell_1$ is added to account for the distance the wave has traveled from the aperture. Considering the probe is replaced with perfect electrical conductor (PEC), its magnetic reflection coefficient is $+1$. Thus, once the returning wave reaches the probe, it reflects back toward the layer's interface with magnitude $-R_\zeta H_\zeta(\rho) e^{-\gamma_{\zeta 1}(z+2\ell_1)}$. Consequently, with each reflection at the PEC, the wave's magnitude becomes twice that of the arriving wave, given that at z=0, the arriving and corresponding reflected waves have identical magnitudes and phase. Subsequently, upon reaching the layer's interface again, part of the wave is reflected back to the probe, and the process continues infinitely.

After the n^{th} reflection from the layer's interface, the magnitude of the differential magnetic wave traveling toward the interface is $(-R_\zeta)^n H_\zeta(\rho) e^{-\gamma_{\zeta 1}(z+2n\ell_1)}$. Finally, it follows that the sum of all these reflected waves at $z = 0$, plus the original radiated wave, is the total differential magnetic wave $\partial H_{\phi t}$ at the aperture, which is given by:

$$\begin{aligned}\partial H_{\phi t}(\rho, z=0) &= H_\zeta(\rho) - 2R_\zeta H_\zeta(\rho) e^{-2\gamma_{\zeta 1}\ell_1} \\ &\quad + 2R_\zeta^2 H_\zeta(\rho) e^{-4\gamma_{\zeta 1}\ell_1} - 2R_\zeta^3 H_\zeta(\rho) e^{-6\gamma_{\zeta 1}\ell_1} \\ &\quad + ... \\ &= \left[1 + 2\sum_{n=0}^{\infty} (-R_\zeta e^{-2\gamma_{\zeta 1}\ell_1})^n\right] H_\zeta(\rho)\end{aligned} \tag{27}$$

The above summation can be expressed as a Taylor series expansion, provided that $R_\zeta e^{-\gamma_{\zeta 1} 2\ell_1} < 1$, which is always the case for non-ideal materials. Considering $R_{a\zeta} = R_\zeta e^{-2\ell\gamma_{\zeta 1}}$, the total differential magnetic wave at the aperture is:

$$\partial H_\phi(\rho, z=0) = \left(\frac{1 - R_{a\zeta}}{1 + R_{a\zeta}}\right) \partial H_{\phi i}\bigg|_{z=0} \tag{28}$$

The above equation shows that the radiated differential magnetic field multiplied by the aggregated reflection coefficient $\frac{1-R_{a\zeta}}{1+R_{a\zeta}}$ is the total differential magnetic field at the aperture. The integral of (28) over ζ is the magnetic field at the aperture considering the effect of the second layer. This can be expressed as:

$$\begin{aligned}H_\phi(\rho, z=0^+) =& j\omega\epsilon_0\epsilon_{m1} \int_a^b E_\rho(\rho')\, \rho' \mathrm{d}\rho' \int_0^\infty \left(\frac{1 + R_{a\zeta}}{1 - R_{a\zeta}}\right. \\ & \left.\frac{J_1(\zeta, \rho) J_1(\zeta, \rho')}{\sqrt{\zeta^2 - k^2}} \zeta\right) \mathrm{d}\zeta\end{aligned} \tag{29}$$

Repeating the steps taken to reach (14) from (12) with the updated magnetic field at aperture when two layers are present, one converges to (16) and (18). However, it is necessary to revise the equation for I_n as follows:

$$I_n = \int_0^\infty \frac{1 + R_{a\zeta}}{1 - R_{a\zeta}} \frac{J_1(\zeta\rho)\zeta}{\sqrt{\zeta^2 - k_1^2}} \cdot \int_a^b f_n(\rho')\, J_1(\zeta\rho')\rho' d\rho' d\zeta \tag{30}$$

This equation can be further simplified to a single integral by integrating over ρ'

$$I_n = \int_0^\infty \frac{1 + R_{a\zeta}}{1 - R_{a\zeta}} \frac{J_1(\zeta\rho)\zeta}{\sqrt{\zeta^2 - k_1^2}} D_n(\zeta)\, d\zeta \tag{31}$$

where $D_n(\zeta)$ is as follows:

$$\begin{aligned}D_n(\zeta) =& \frac{2}{\pi} \frac{N_n}{p_n} \frac{1}{J_0(p_n b)} \frac{\zeta}{p_n^2 - \zeta^2} \cdot \\ & [J_0(\zeta b) J_0(p_n a) - J_0(\zeta a) J_0(p_n b)] \qquad n > 0 \\ D_0(\zeta) =& \frac{1}{\sqrt{\ln(b/a)}} \frac{1}{\zeta} [J_0(\zeta a) - J_0(\zeta b)] \qquad n = 0\end{aligned} \tag{32}$$

Using this updated equation, the normalized weight reflection coefficients W_n of two-layer material can be determined. Of particular interest in (16) is the primary mode reflection coefficient R_0. The primary mode is the only mode that propagates along the z-axis, and its reflection coefficient R_0 is the parameter measured experimentally using a VNA. However, R_0 cannot be directly determined from (16) due to the presence of an infinite number of unknown higher-order reflection coefficients R_n.

In the following section the point-matching approach is presented, which is used to extract a system of multiple equations from (16) allowing one to solve for R_0.

IV. REFLECTION COEFFICIENT THROUGH POINT MATCHING

Up to this point, the normalized weighted reflection coefficients for both single-layer and two-layer materials are given for all modes at a specific radial position ρ at the aperture, from which R_0 needs to be determined. One approach to achieving this goal is the point-matching method described in the following subsection.

In order to determine R_0 from (16), it is necessary to truncate the number of considered modes to N. When dealing with a multi-variable problem, an equal number of equations as the number of modes being considered is required. Two

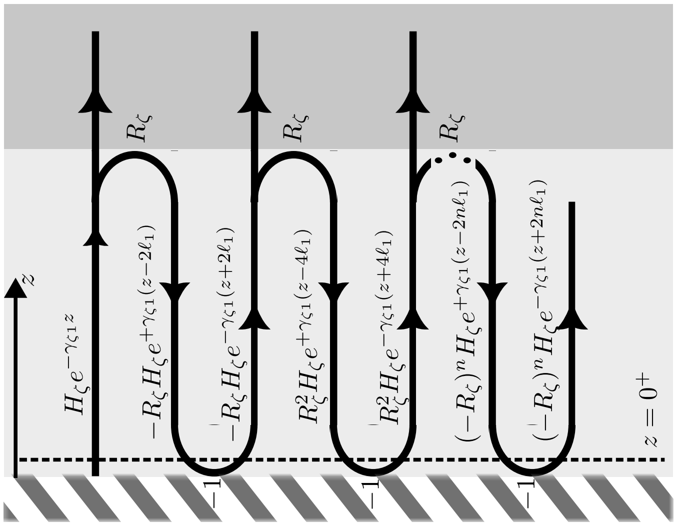

Fig. 2. Reflection diagram illustrating the interaction of a radiated magnetic wave between the interface and a perfect electrical conductor (PEC). The incident magnetic wave at the aperture is ∂H_i. Upon reaching the material interface, it reflects back with a reflection coefficient of $-R_\zeta$. The reflected wave then travels back to the PEC as $-R_\zeta H_\zeta e^{\gamma_{\zeta 1}(z-2\ell_1)}$. Subsequently, it undergoes repeated complete reflections from the PEC. After a total of n reflections, the resulting wave is $(-R_\zeta)^n H_\zeta e^{-\gamma_{\zeta 1}(z+2n\ell_1)}$.

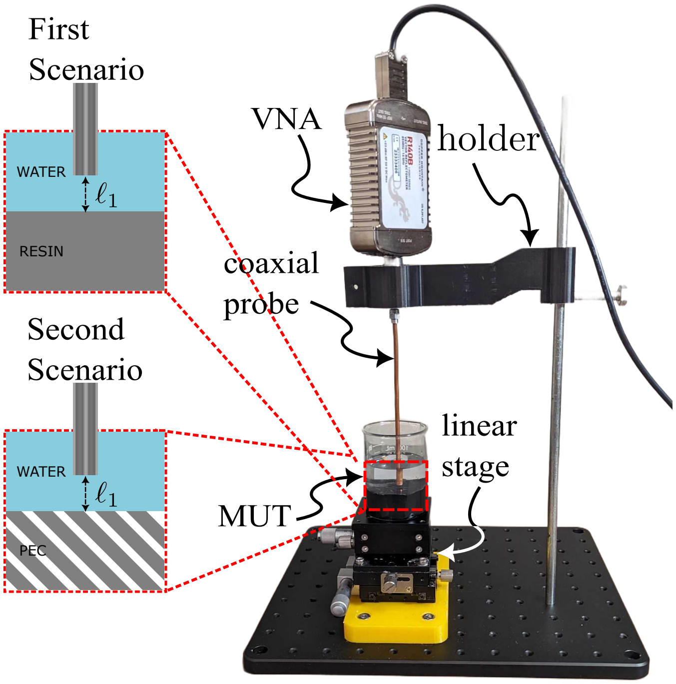

Fig. 3. Experimental setup used to validate the proposed model: The aperture of open-ended coaxial probe connected to a VNA is emerged in a 2-layer MUT. The latter rests on a linear stage that can move vertically, allowing the distance ℓ_1 between the probe's aperture and the MUT layer interface to be controlled with 10 μm increments. Two experimental scenarios with different MTU are used: one with water on top of resin, and the another with water on top of a PEC.

methods have been proposed in the literature to obtain these equations from (16). One of these methods is Galerkin's method, which involves multiplying both sides of (16) by basis functions $f_n(\rho)$ and then integrating both sides over the range from a to b [23]. Upon integration, the dependency on ρ is eliminated. The integration process can be simplified by utilizing the orthogonality identity of Bessel functions. Nevertheless, this method remains computationally intensive as it involves calculating three-dimensional integrals numerically.

The second method, which is the one employed in this paper, is the point-matching method [21], [32], [33]. This approach involves deriving multiple equations by selecting different matching points (ρ_i) in (16). By doing so, the computational cost can be reduced, as the solution does not rely on three-dimensional integrals. This can be done by dividing the space between a and b (See Fig. 1 (c)) into N equal segments and matching points in the middle of each segment. Additionally, [21] suggests that for faster convergence of the multi-variable problem, the points can be determined based on the arithmetic mean of both the internal and external distributions as follow:

$$\rho_i = a + \frac{b-a}{2}\left[\frac{i-1}{N-1} + \frac{2i-1}{2N}\right], \quad i = 1, 2, \cdots, N \quad (33)$$

Equation (33) gives a set of matching points ρ_i that when substituted into (16) form a system of N equations. Solving this system of questions yields the reflection coefficients R_n for mode $n = 0$ up to mode $n = N$, providing a solution to the forward problem, that is, determining the reflection coefficient R_0 for a probe inside a one or a two-layer material. An advantage of the proposed method compared to [23], [27] is that it requires N fewer infinite integrals over continuous eigenvalues ζ compared to other two-layer models, for the same number of considered modes. The inverse problem, i.e., determining the permittivity of a layer given R_0, typically involves multiple iterations of the forward model. Therefore, simplifying the forward model substantially decreases the overall computational time required to obtain a solution for the inverse problem, making it ideal for real-time measurements.

In the next section, the forward model will be validated experimentally in two different scenarios. Additionally, to demonstrate the utility of the model in practical applications, the model is implemented in an inverse problem that estimates the permittivity of one layer, or the distance from the second layer (ℓ_1), based on the measured reflection coefficient.

V. EXPERIMENTAL RESULTS

The experimental setup used to validate the model is shown in Fig. 3. A standard 50 Ω semi-rigid coaxial probe (RG402 from L-com), with a dielectric radius of $b = 0.15$ mm and an inner conductor radius of $a = 0.46$ mm, is directly connected to a R104B vector network analyzer (VNA) from Copper Mountain. The VNA measures the reflection coefficient (R_0) of a 2-layer MUT placed near the probe's aperture. Connecting the probe directly to the VNA minimizes discrepancies between the measured reflection coefficient and the actual reflection coefficient observed at the aperture of the probe. In order to eliminate coaxial probe length and interconnection influences, the same technique explained in [20] is used for calibration of VNA and probe using tests performed with air, water, and ethanol [34].

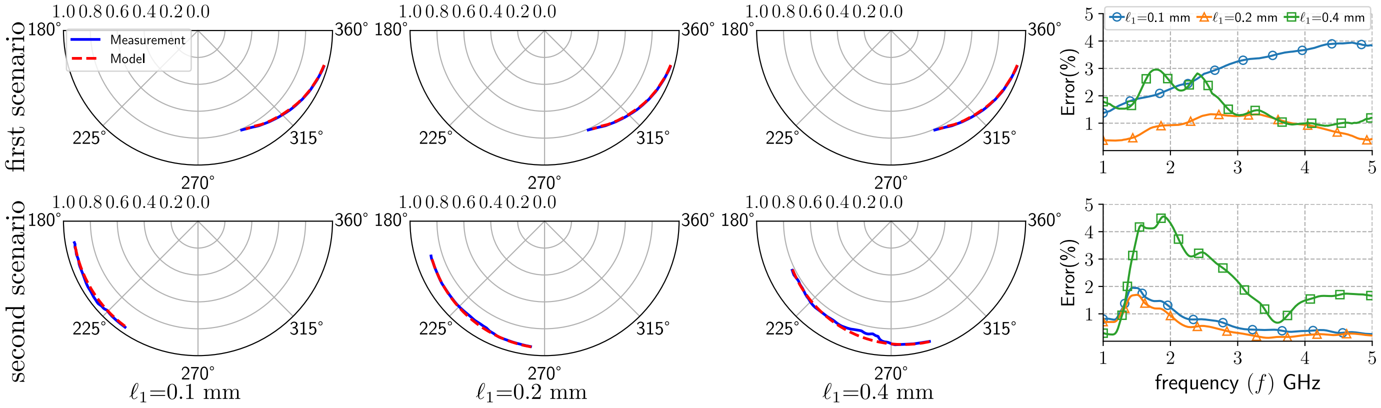

Fig. 4. Measured *vs* model-predicted reflection coefficient at 3 fixed distances $\ell_1 = 0.1$ mm, 0.2 mm, and 0.4 mm from the MTU interface in the first scenario (water/resin) and second scenario (water/PEC): points on each of the 6 polar plots on the left corresponds to one of the 201 measurement frequencies spanning 1 GHz to 5 GHz. The measurement (solid) and model (dashed) results show good consistency. The last column on the right shows the relative error between the model and the measurements for an average error of 1.75%. The first and second rows correspond to the first and second scenarios, respectively.

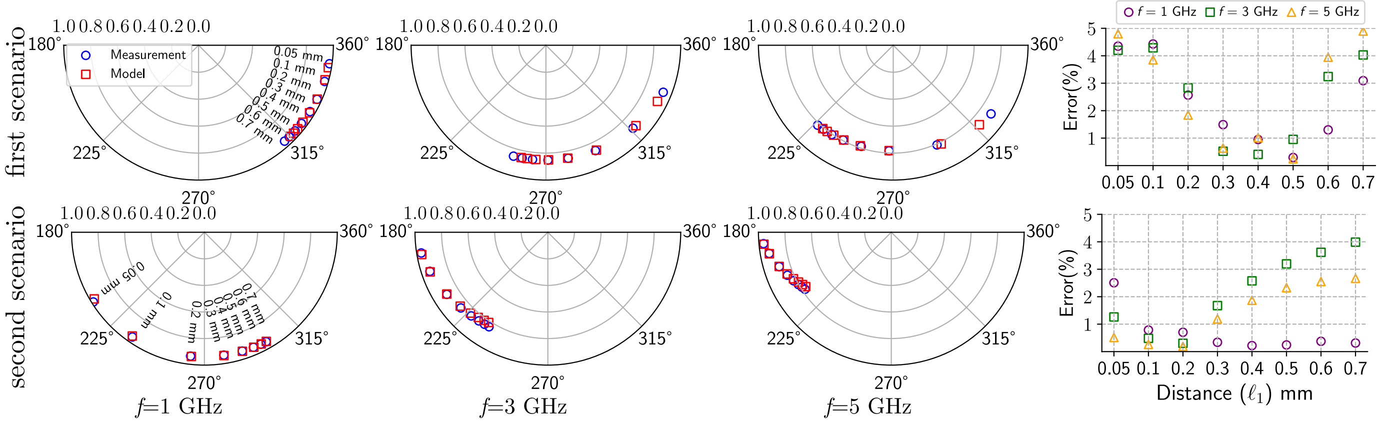

Fig. 5. Measured *vs* model-predicted reflection coefficient at 3 fixed frequencies $f = 1$ GHz, 3 GHz, and 5 GHz in the first scenario (water/resin) and second scenario (water/PEC): Every point on each of the 6 polar plots on the left corresponds to one of the 8 considered distances ℓ_1 between the probe's aperture and the MTU layer interface spanning 0.05 mm to 0.70 mm. The last column on the right shows the relative error between the model and the measurements for an average error of 1.85%. The first and second rows correspond to the first and second scenario, respectively.

A. *Experimental Scenarios*

The MUT is composed of two layers of different materials of known permittivity placed on top of one another inside of a glass container. The probe's aperture is initially immersed in the top layer of the MUT at a distance of ℓ_1 from the bottom layer. The container rests on top of a linear stage that can move vertically in steps of 10 μm. This allows the MUT to be translated vertically while the probe is held in place, thereby changing the distance ℓ_1 between the probe's aperture to the second layer of the MUT.

Two different MUT are considered:

- First scenario: Distilled water (with relative permittivity $73 \leq \epsilon_{r1} \leq 78$) and liquid resin (Formlabs' V4) (with relative permittivity $3.4 \leq \epsilon_{r2} \leq 4.4$) are used as the top and bottom layers of the MUT, respectively. The probe's aperture is initially placed in the higher permittivity material, and by raising the linear stage, the probe moves toward a lower permittivity material; The permittivity of the resin was measured using the single-layer model we proposed in [20].
- Second scenario: Distilled water (with relative permittivity $73 \leq \epsilon_{r1} \leq 78$) and a perfect electric conductor (aluminum puck) are used as the top and bottom layers of the MUT, respectively. In contrast to Scenario 1, by raising the linear stage the probe's aperture moves toward a higher permittivity material.

As a starting point, a reference initial distance ℓ_1 between the probe's aperture and the interface between the two materials of the MUT needs to be determined. The initial distance should be within the probe's penetration depth so that the bottom layer of the MTU does have an influence on the measured reflection coefficient. Considering that the probe's penetration depth is approximately equal to its diameter [30], [35], an initial distance of $\ell_1 = 0.3$ mm is chosen. To circumvent the fact that there is no way to physically measure the distance ℓ_1, the probe is initially placed close to the second layer ($\ell_1 > 0$) and the reflection coefficient is measured. Model fit is then used to determine the correct initial distance ℓ_1. A few iterations are performed where the position of the probe is adjusted until the model outputs the desired initial distance. This process is only executed once, and subsequently the linear stage is used to move the MTU container vertically with respect to the initial position.

The VNA measures the reflection coefficient of the MUT from $\ell_1 = 0.7$ mm to $\ell_1 = 0.1$ mm in 0.1 mm intervals, with an additional step at $\ell_1 = 0.05$ mm at a frequency ranging from 1 GHz to 5 GHz, sampled at 20 MHz intervals for a total of 201 individual frequencies.

B. Forward Model Validation Results

To validate the forward model, the frequency, the distance ℓ_1, and the permittivity of both MUT layers are input to the model and the estimated reflection coefficient is then compared to the measured reflection coefficient. A Python script was developed to compute the reflection coefficient across the same measurement scenarios based on the proposed model. The *Quad* function from the *SciPy* library is employed to determine the numerical integration of I_n values. The inner integral's range over ζ in (31), initially set to infinity, is confined to 10^5. The calculation is constrained to five modes, i.e., $n = 5$ in (16) chosen based on recommendations from prior research on the one-layer model [21]. Consequently, the determination of R_0 involves solving a system of 5 linear equations, executed through the *Solve* function from the *Numpy* library.

Fig. 4 and 5 compare the measured reflection coefficient with the model-predicted reflection coefficient for various frequencies and distances ℓ_1. Fig. 4 shows the results across the entire frequency bandwidth at three fixed distances of $\ell_1 = 0.1$, 0.2, and 0.4 mm. Each point on the polar plot corresponds to a specific frequency. In the first scenario, the model shows an error of less than 1% at 1 GHz compared to the true measurements. The observed error increases slightly with the frequency but does not exceed 3% for an average error of 1.8 % across all 804 measurements. For the second scenario, the error is under 2% for $\ell_1 = 0.1$ mm and $= 0.2$ mm for the entire frequency bandwidth. While the error reaches 5% between 1.5 GHz and 2.5 GHz for $\ell_1 = 0.4$ mm, the average error is 3.5 % across all measurement points.

Fig. 5 shows the results across all measured ℓ_1 distances at 3 fixed frequencies of 1 GHz, 3 GHz and 5 GHz. Each point on the polar plot corresponds to a specific distance ℓ_1. The average errors observed in scenarios 1 and 2 over all 1608 measurements are 1.8 % and 1.7 % respectively.

The primary source of error, notably evident in the first scenario, arises from uncertain measurements of the resin's properties at high frequencies as there are no data available in the literature to validated the measured result. Another potential error source in the first scenario is the presence of solvents in the resin, affecting both water and resin permittivity values. Additionally, VNA and probe calibration may further contribute to the observed errors in both scenarios. For example, differences in material properties used for calibration and the actual experiment could lead to imprecise calibration. Finally, uncertainties in the linear stage position measurement might also contribute to errors. Despite these potential error sources, the proposed model exhibits strong consistency with the measured results.

TABLE I
PERMITTIVITY ESTIMATION ERROR OF WATER IN SCENARIO 1 (RESIN)

Model	distance ℓ_1 from second layer		
	0.1 mm	0.2 mm	0.4 mm
Single-layer [21]	72.1%	56.2%	32.6%
dProposed two-Layer	1.36%	0.87%	1.08%

C. Inverse Model Validation Results

In the previous subsection, the model is used to calculate the reflection coefficient R_0 for a given combination of ϵ_{m1}, ϵ_{m2}, and ℓ_1. Another method deployed to validate the proposed model, which has many applications in biomedical spectroscopy [36]–[39], is to use the model in an inverse problem. The inverse problem entails determining the model parameters (such as ℓ_1, ϵ_{m1}, and ϵ_{m2}) necessary to match a measurement, in this case, R_0. In the context of a multilayered medium, one application involves determining the distance ℓ_1 between the probe tip and the interface, or the permittivity ϵ_m, given other parameters as inputs.

In [34], a Newton-Raphson method is used to extract the permittivity of single-layer materials. This study employs a similar technique with some modifications to address the two-layer problem. To do so, let R_0 be represented by the multivariable function $R(\epsilon_{m1}, \epsilon_{m2}, \ell_1)$. The frequency and other model constants are omitted for simplicity of notation. If the measured reflection coefficient is R_{0m}, then the unknown parameter, e.g., ℓ_1 or ϵ_{m1}, is the root of:

$$F(\epsilon_{m1}, \epsilon_{m2}, \ell_1) = R(\epsilon_{m1}, \epsilon_{m2}, \ell_1) - R_{0m} \tag{34}$$

It should be noted $\epsilon_{m1}, \epsilon_{m2} \in \mathbb{C}$, while $\ell_1 \in \mathbb{R}$. Assuming a current estimation of, for example $\ell_{1(i)}$, the following approximation holds true for an iterative improved estimation:

$$\begin{aligned} &F(\epsilon_{m1}, \epsilon_{m2}, \ell_{1(i+1)}) = F(\epsilon_{m1}, \epsilon_{m2}, \ell_{1(i)}) + \\ &(\partial F/\partial \ell_1)_{(i)} \Delta \ell_{1(i)} = 0 \end{aligned} \tag{35}$$

where $\Delta \ell_{1(i)}$ is the increment value. Rearranging the aforementioned equation yields:

$$\Delta \ell_{1(i)} = -\frac{F(\epsilon_{m1}, \epsilon_{m2}, \ell_{1(i)})}{(\partial F/\partial \ell_1)_{(i)}} \tag{36}$$

the updated ℓ_1 then would be:

$$\ell_{1(i+1)} = \ell_{1(i)} + \Delta \ell_{1(i)} \tag{37}$$

Fig. 6 compares the estimated distance ℓ_1 using the inverse problem with the measured distance for the two scenarios across the entire frequency range for an average error of 10 μm.

Through the same procedure the permittivity values can be extracted when other parameters are know by setting:

$$\Delta \epsilon_{m1(i)} = -\frac{F(\epsilon_{m1}, \epsilon_{m2}, \ell_{1(i)})}{(\partial F/\partial \epsilon_{m1})_{(i)}} \tag{38}$$

$$\epsilon_{m1(i+1)} = \epsilon_{m1(i)} + \Delta \epsilon_{m1(i)} \tag{39}$$

The real part of the estimated permittivity of the first layer ϵ_{m1} in Scenario 1 is presented in Fig. 7 along with its

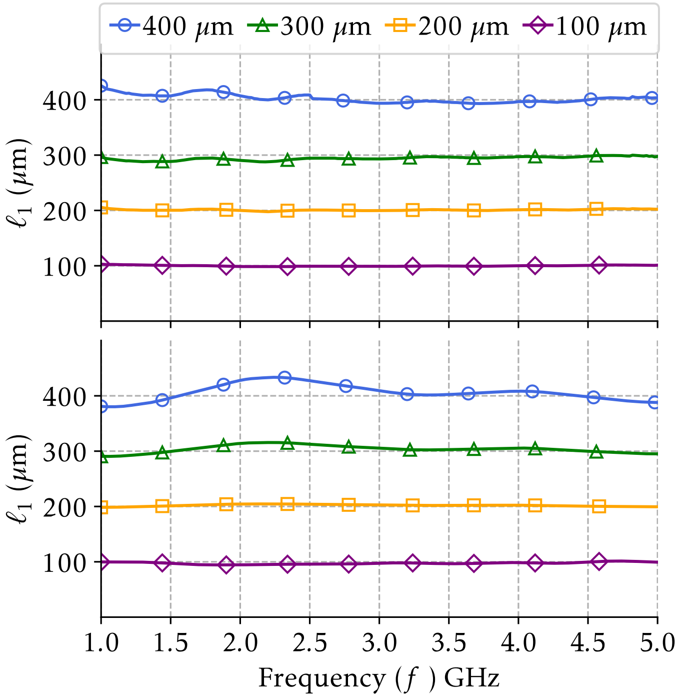

Fig. 6. Estimated distance between the probe aperture to the second layer ℓ_1 the using the inverse problem in water/resin and water/PEC scenarios. For example, at a measured distance of 400μ (blue) the ideal estimated distance would correspond to a straight line at 400μ spanning the entire frequency bandwidth. The average error for all 1608 extracted points is 10 μm.

measured permittivity fitted through a Cole-Cole model. To demonstrate how the proposed model enhances the accuracy of permittivity measurement, also included in this figure is the extracted permittivity using the single-layer model for $\ell_1 = 0.4$ mm. The average error for both models for all measured distances is provided in Table I. Notably, even at a distance of $\ell_1 = 0.4$ mm, where the second layer is situated approximately at half of the penetration depth of the probe, the permittivity of the second layer substantially affects the measured permittivity. Without considering the effect of the second layer, the observed error is 32.6%, whereas with the proposed model the error is 1.08%.

VI. CONCLUSION

While most applications of permittivity spectroscopy involve heterogeneous materials, previous works on modelling open-ended coaxial probes often assume the medium to be made of a single layer of an homogeneous material. This paper proposes a novel method to model the reflection coefficient of an open-ended coaxial probe in layered media. The model considers the reflection coefficient of all medium layers in a full-wave reflection model. In contrast to other methods, spherical waves are expanded to plane waves using the sommerfeld identity. This results oblique incident to the interface to be replaced with normal incident. Radiation from the aperture to second layer occurs in oblique incident. This alteration simplifies the calculation of the reflection coefficient from the second layer. The overall proposed model offers a simpler formulation than a few existing models while maintaining accuracy.

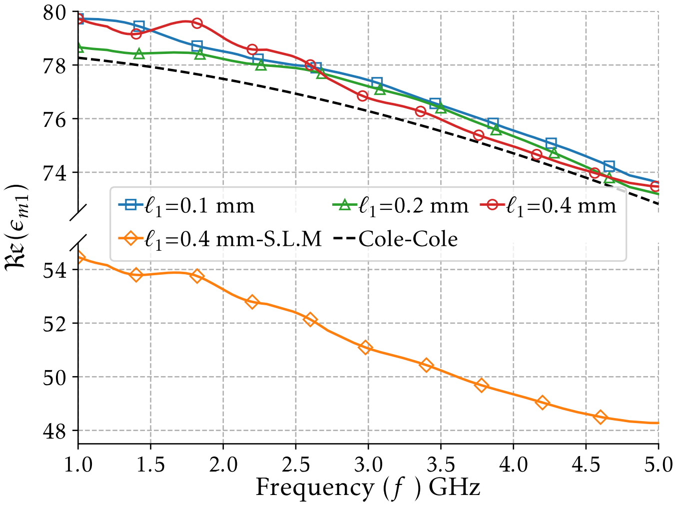

Fig. 7. The real part of the extracted permittivity of the first layer (water, ϵ_{m1}) for the first scenario (water/resin) at three distances $\ell_1 = 0.1$ mm, 0.2 mm, and 0.4 mm using the proposed model, along with the result at $\ell_1 = 0.4$ mm using the single-layer model. Additionally, the Cole-Cole model of water is presented for reference.

Two experimental scenarios are considered to validate the model's ability to correctly estimate the reflection coefficient of a two-layer material. In these experiments, the probe's aperture is placed near the interface between the two tissue layers and within the penetration depth of the coaxial probe. In this specific region, the second layer influences the reflection coefficient seen by the probe. The results obtained in the experimental scenarios across a total of 1608 measurement points show that the model can accurately predict the reflection coefficient. These measurements are further used in an inverse problem to estimate both the distance ℓ_1 and the permittivity ϵ_{m1} of the first layer. While ignoring the second layer (using a single-layer model) results in inaccurate outcomes, the results obtained using the proposed model, when compared with the Cole-Cole model of water, shows remarkable accuracy.

The proposed model has several practical applications. For example, a major challenge in using coaxial probes for spectroscopy of solid materials is to deal with the air gap between probe tip and the MUT, which can strongly affect the measured reflection coefficient. With the proposed model, if a fixed and controlled air gap is maintained, the effect of the latter on the reflection coefficient can be taken into account. Furthermore, the proposed model can be employed for permittivity measurement of heterogeneous materials such as biological specimens. Especially in these applications, real-time measurement is essential. The low computational requirements of this method, while maintaining the accuracy of the full-wave, provide a distinct advantage compared to a few other proposed methods.

REFERENCES

[1] M. Lu, X. Xiao, Y. Pang, G. Liu, and H. Lu, "Detection and localization of breast cancer using uwb microwave technology and cnn-lstm framework," *IEEE Trans. Microw. Theory Techn.*, vol. 70, no. 11, pp. 5085–5094, Oct. 2023.

[2] M. Asefi, A. Baran, and J. LoVetri, “An experimental phantom study for air-based quasi-resonant microwave breast imaging,” *IEEE Trans. Microw. Theory Techn.*, vol. 67, no. 9, pp. 3946–3954, Sept. 2019.

[3] H. Banting and C. E. Saavedra, “Dielectric spectroscopy of fluids and polymers for microwave microfluidic circuits and antennas,” *IEEE Trans. Microw. Theory Techn.*, vol. 69, no. 1, pp. 337–343, Jan. 2021.

[4] J. Sorocki, K. Wincza, S. Gruszczynski, and I. Piekarz, “Direct broadband dielectric spectroscopy of liquid chemicals using microwave-fluidic two-wire transmission line sensor,” *IEEE Trans. Microw. Theory Techn.*, vol. 69, no. 5, pp. 2569–2578, May 2021.

[5] A. Martellosio, M. Pasian, M. Bozzi, L. Perregrini, A. Mazzanti, F. Svelto, P. E. Summers, G. Renne, L. Preda, and M. Bellomi, “Dielectric properties characterization from 0.5 to 50 ghz of breast cancer tissues,” *IEEE Trans. Microw. Theory Techn.*, vol. 65, no. 3, pp. 998–1011, March 2017.

[6] B. Filali, F. Boone, J. Rhazi, and G. Ballivy, “Design and calibration of a large open-ended coaxial probe for the measurement of the dielectric properties of concrete,” *IEEE Trans. Microw. Theory Techn.*, vol. 56, no. 10, pp. 2322–2328, Oct. 2008.

[7] D. Berube, F. Ghannouchi, and P. Savard, “A comparative study of four open-ended coaxial probe models for permittivity measurements of lossy dielectric/biological materials at microwave frequencies,” *IEEE Trans. Microw. Theory Techn.*, vol. 44, no. 10, pp. 1928–1934, Oct. 1996.

[8] D. L. Gershon, J. Calame, Y. Carmel, T. Antonsen, and R. M. Hutcheon, “Open-ended coaxial probe for high-temperature and broad-band dielectric measurements,” *IEEE Trans. Microw. Theory Techn.*, vol. 47, no. 9, pp. 1640–1648, Sept. 1999.

[9] P. De Langhe, L. Martens, and D. De Zutter, “Design rules for an experimental setup using an open-ended coaxial probe based on theoretical modelling,” *IEEE Trans. Instrum. Meas.*, vol. 43, no. 6, pp. 810–817, Dec. 1994.

[10] G. B. Gajda and S. S. Stuchly, “Numerical analysis of open-ended coaxial lines,” *IEEE Trans. Microw. Theory Techn.*, vol. 31, no. 5, pp. 380–384, May 1983.

[11] G. Chen, K. Li, and Z. Ji, “Bilayered dielectric measurement with an open-ended coaxial probe,” *IEEE Trans. Microw. Theory Techn.*, vol. 42, no. 6, pp. 966–971, June 1994.

[12] M. Shao, X. Li, Z. Liu, X. Liang, L. Lin, H. Fan, and J. Xu, “Time domain calibration method of open-ended coaxial probe in dielectric measurement,” *IEEE Trans. Instrum. Meas.*, vol. 71, pp. 1–8, 2022.

[13] T. W. Athey, M. A. Stuchly, and S. S. Stuchly, “Measurement of radio frequency permittivity of biological tissues with an open-ended coaxial line: Part i,” *IEEE Trans. Microw. Theory Techn.*, vol. 30, no. 1, pp. 82–86, 1982.

[14] T. Marsland and S. Evans, “Dielectric measurements with an open-ended coaxial probe,” in *Proc. Inst. Elect. Eng.—Microw., Antennas, Propag.*, vol. 134, no. 4. IET, 1987, pp. 341–349.

[15] M. A. Stuchly, M. M. Brady, S. S. Stuchly, and G. Gajda, “Equivalent circuit of an open-ended coaxial line in a lossy dielectric,” *IEEE Trans. Instrum. Meas.*, no. 2, pp. 116–119, June 1982.

[16] D. Popovic, L. McCartney, C. Beasley, M. Lazebnik, M. Okoniewski, S. C. Hagness, and J. H. Booske, “Precision open-ended coaxial probes for in vivo and ex vivo dielectric spectroscopy of biological tissues at microwave frequencies,” *IEEE Trans. Microw. Theory Techn.*, vol. 53, no. 5, pp. 1713–1722, May 2005.

[17] D. Misra, “On the measurement of the complex permittivity of materials by an open-ended coaxial probe,” *IEEE Microwave and Guided wave lett.*, vol. 5, no. 5, pp. 161–163, May 1995.

[18] D. V. Blackham and R. D. Pollard, “An improved technique for permittivity measurements using a coaxial probe,” *IEEE Trans. Instrum. Meas.*, vol. 46, no. 5, pp. 1093–1099, Oct. 1997.

[19] D. K. Misra, “A quasi-static analysis of open-ended coaxial lines (short paper),” *IEEE Trans. Microw. Theory Techn.*, vol. 35, no. 10, pp. 925–928, Oct. 1987.

[20] H. A. Bidgoli, N. Schieda, and C. Rossa, “On the sensitivity of bevelled and conical coaxial needle probes for dielectric spectroscopy,” *IEEE Trans. Instrum. Meas.*, 2023.

[21] J. R. Mosig, J.-C. E. Besson, M. Gex-Fabry, and F. E. Gardiol, “Reflection of an open-ended coaxial line and application to nondestructive measurement of materials,” *IEEE Trans. Instrum. Meas.*, no. 1, pp. 46–51, March 1981.

[22] S. A. R. Naqvi, A. T. Mobashsher, B. Mohammed, D. Foong, and A. Abbosh, “Benign and malignant skin lesions: Dielectric characterization, modelling and analysis in frequency band 1 to 14 ghz,” *IEEE Trans. Biomed. Eng.*, Feb. 2022.

[23] C.-L. Li and K.-M. Chen, “Determination of electromagnetic properties of materials using flanged open-ended coaxial probe-full-wave analysis,” *IEEE Trans. Instrum. Meas.*, vol. 44, no. 1, pp. 19–27, Feb. 1995.

[24] M. Wu, X. Yao, and L. Zhang, “An improved coaxial probe technique for measuring microwave permittivity of thin dielectric materials,” *Meas. Sci. Technol.*, vol. 11, no. 11, p. 1617, 2000.

[25] A. Aimoto and T. Matsumoto, “Noninvasive method for measuring the electrical properties of deep tissues using an open-ended coaxial probe,” *Med. Eng. Phys.*, vol. 18, no. 8, pp. 641–646, 1996.

[26] L. L. Li, N. Ismail, L. Taylor, and C. Davis, “Flanged coaxial microwave probes for measuring thin moisture layers,” *IEEE Trans. Biomed. Eng.*, vol. 39, no. 1, pp. 49–57, Jan 1992.

[27] J. Baker-Jarvis, M. D. Janezic, P. D. Domich, and R. G. Geyer, “Analysis of an open-ended coaxial probe with lift-off for nondestructive testing,” *IEEE Trans. Instrum. Meas.*, vol. 43, no. 5, pp. 711–718, Oct. 1994.

[28] J. Galejs, *Antennas in Inhomogeneous Media: International Series of Monographs in Electromagnetic Waves*. Elsevier, 2013, vol. 15.

[29] R. S. Elliot, *Antenna theory and design*. John Wiley & Sons, 2006.

[30] H. A. Bidgoli, N. Schieda, and C. Rossa, “Penetration depth quantification of open-ended coaxial probes for dielectric spectroscopy of layered media,” in *Proc. 2023 IEEE Can. Conf. Electron. Comp. Eng.* IEEE, 2023, pp. 94–98.

[31] D. M. Pozar, *Microwave engineering*. John wiley & sons, 2011.

[32] S. Bakhtiari, S. I. Ganchev, and R. Zoughi, “Analysis of radiation from an open-ended coaxial line into stratified dielectrics,” *IEEE Trans. Microw. Theory Techn.*, vol. 42, no. 7, pp. 1261–1267, July 1994.

[33] K. Folgerø, K. Haukalid, J. Kocbach, and A. S. Peterson, “Combined thickness and permittivity measurement of thin layers with open-ended coaxial probes,” *Sensors*, vol. 19, no. 8, p. 1765, 2019.

[34] J. Grant, R. Clarke, G. Symm, and N. M. Spyrou, “A critical study of the open-ended coaxial line sensor technique for rf and microwave complex permittivity measurements,” *J. Phys. E: Sci. Instrum.*, vol. 22, no. 9, p. 757, 1989.

[35] P. M. Meaney, A. P. Gregory, J. Seppälä, and T. Lahtinen, “Open-ended coaxial dielectric probe effective penetration depth determination,” *IEEE Trans. Microw. Theory Techn.*, vol. 64, no. 3, pp. 915–923, March 2016.

[36] I. Dilman, M. N. Akinci, T. Yilmaz, M. Çayören, and I. Akduman, “A method to measure complex dielectric permittivity with open-ended coaxial probes,” *IEEE Trans. Instrum. Meas.*, vol. 71, pp. 1–7, 2022.

[37] S. A. R. Naqvi, M. Manoufali, B. Mohammed, A. T. Mobashsher, D. Foong, and A. M. Abbosh, “In vivo human skin dielectric properties characterization and statistical analysis at frequencies from 1 to 30 ghz,” *IEEE Trans. Instrum. Meas.*, vol. 70, pp. 1–10, 2020.

[38] A. Mirbeik-Sabzevari and N. Tavassolian, “Tumor detection using millimeter-wave technology: Differentiating between benign lesions and cancer tissues,” *IEEE Microw. Mag.*, vol. 20, no. 8, pp. 30–43, Aug. 2019.

[39] A. Mirbeik-Sabzevari, R. Ashinoff, and N. Tavassolian, “Ultra-wideband millimeter-wave dielectric characteristics of freshly excised normal and malignant human skin tissues,” *IEEE Trans. Biomed. Eng.*, vol. 65, no. 6, pp. 1320–1329, June 2017.

Hossein Asilian Bidgoli is a Ph.D. student in System and Computer Engineering at Carleton University, Ottawa, Canada. He received the B.Sc. degree from Isfahan University of Technology, Isfahan, Iran, and the M.Sc. degree from Iran University of Science and Technology, Tehran, Iran, all in electrical engineering. His research interests include biomedical applications of microwave spectroscopy, electromagnetic parametric modelling and design, optimization algorithms, deep neural networks, and microwave circuits design and analysis.

Nicola Schieda is an abdominal radiologist at the Ottawa hospital and an Associate Professor in Radiology and Surgery at the University of Ottawa. He is the Director of Abdominal and Pelvic MRI and Prostate Imaging at the Ottawa hospital. He is a member of the Scientific Subcommittees for Genitourinary Imaging at the Radiological Society of North America, American Roentgen Ray Society and Society of Abdominal Radiology. He is a panel member of the American College of Radiology Appropriateness Criteria for Urological Imaging, a member of the Society of Abdominal Radiology Disease and is the Chair of the American College of Radiology Genitourinary Continuing Professional Improvement program. His current research interests include imaging of Genito-urinary malignancies and body MRI applications.

Carlos Rossa is an Associate Professor in the Department of Systems and Computer Engineering at Carleton University. He received his B.Eng. and M.Sc. degrees in Mechanical Engineering from the Ecole Nationale d'Ingénieurs de Metz, Metz, France, and earned his PhD degree in Mechatronics and Robotics from the Sorbonne Université (UPMC), Paris, France, under the auspices of the Commissariat à l'Energie Atomique (CEA). His research interests include biomedical instrumentation, medical robotics, and image-guided percutaneous surgery.